Journal of Materials Chemistry B

PAPER

View Article Online
View Journal | View Issue

Cite this: J. Mater. Chem. B, 2019, 7, 5873

A ZnO–curcumin nanocomposite embedded hybrid collagen scaffold for effective scarless skin regeneration in acute burn injury†

Cheirmadurai Kalirajan[ab] and Thanikaivelan Palanisamy *[ab]

Received 31st May 2019,
Accepted 23rd August 2019

DOI: 10.1039/c9tb01097a

rsc.li/materials-b

Scar formation in severe burn injury is a major health concern. Herein, we developed a hybrid collagen scaffold with an incorporated ZnO–curcumin nanocomposite, which facilitates scarless wound healing. Biocompatibility and hemocompatibility studies unveiled that the hybrid scaffold is apt for *in vivo* wound healing studies. Histological and immunohistochemical analyses demonstrate that the hybrid scaffold accelerated scarless burn wound healing in albino rats owing to the ZnO–curcumin nanocomposite induced up-regulation of angiogenesis and TGF-β3 expression. The semi-quantitatively measured scar elevation index of the hybrid scaffold-treated animals is on a par with that of the unwounded or normal skin. The studies suggest that the prepared hybrid biomaterial could be a potential candidate for scarless healing in severe burn injuries.

Introduction

Skin is the largest organ of the body and it protects the internal organs and tissues from exterior environmental factors. The epidermis, dermis and hypodermis are the three basic layers of the skin, which may be injured by burns, physical trauma, surgery and others.[1] Upon such damage, the human body initializes a set of subsequent responses to restore the structure and functions of the normal skin. The healing process is more complex as it involves a cascade of molecular events such as inflammation, granulation tissue formation, re-epithelialization, formation of new extracellular matrices and tissue remodeling.[2] Among other injuries, burn injuries are found to cause severe damage and in some cases may lead to death. Burns result from exposure to heat, radiation and other chemical agents. Based on the severity and depth of the wound, burn injury is classified into first, second and third degree burns. The first-degree burn is a minor form of injury and it does not require any medical treatment, which will heal automatically. The second and third degree burn damage up to the dermis or the muscle layer of the skin, and the patients require continuous medical treatment to heal and restore the skin function.[3] Burn injury accompanied by orthopedic, neurologic and metabolic problems renders the healing process more complicated. These physiological challenges can also lead to poor healing and excessive scar formation.[4] Furthermore, the healing time is prolonged due to some other factors including inflammation, infection, *etc.* The prolonged healing time is linearly related to inferior skin regeneration and scar formation. More research initiatives are needed to overcome the big challenges persisting in chronic burn wound healing and to improve healing efficiency. Recent developments such as tissue transplantation from the same body to defective sites and tissue engineering using dermal–epidermal skin substitutes are being employed to treat severe burn injury.[5–7] Nevertheless, these methods have limitations such as donor-site shortage, propensity to contraction and scarring. Therefore, a search for new therapeutic agents that can reduce infections, support the wound healing process and provide pain relief is receiving more interest.

Collagen is the major structural protein found in the extra cellular matrix (ECM) of skin and various connective tissues. The biocompatibility, biodegradation and low antigenicity properties of collagen-based scaffolds make them a potential candidate for tissue regeneration.[8,9] Furthermore, it is structurally similar to the natural ECM and has been demonstrated to repair various soft and hard tissues successfully.[10,11] Collagen based scaffolds are able to absorb wound exudates and maintain a moisture environment in the wound bed, which helps in cell migration and skin regeneration. However, the stability of collagen in the enzymatic environment of wounds is very low, which makes cross-linking essential. Aldehyde-based chemical cross-linkers such as glutaraldehyde have been used for a long time in the field of tissue engineering to stabilize the collagen molecule and recent studies on these chemical cross-linkers

[a] Advanced Materials Laboratory, Central Leather Research Institute (Council of Scientific and Industrial Research), Adyar, Chennai 600020, India. E-mail: thanik8@yahoo.com, thanik@clri.res.in
[b] University of Madras, Chepauk, Chennai 600005, India

† Electronic supplementary information (ESI) available. See DOI: 10.1039/c9tb01097a

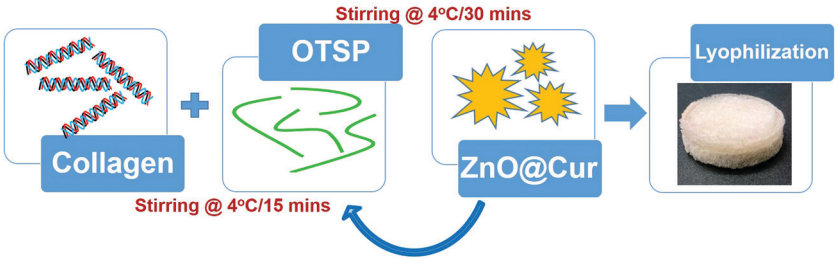

Scheme 1 Schematic showing the preparation of the hybrid scaffolds.

prove that they are cytotoxic to cells.[12] To overcome these problems, researchers are exploring non-cytotoxic natural cross-linkers such as chemically modified polysaccharides for stabilizing collagen molecules.[13–15] Tamarind seed polysaccharide (TSP) is extracted from the seeds of *Tamarindus indica* L., a common tree found in India and South East Asia, belonging to the family Leguminosae. The polysaccharide (TSP) consists of β(1–4)-D-glucan as its backbone and most of them are substituted with side chains of (1–6) linked α-xylopyranose to glucose residues. TSP is biocompatible and it is used as a binder, and a gelling, emulsifying and suspending agent in many pharmaceutical formulations.[16,17]

Preparation of hybrid scaffolds to overcome all the persisting problems has been gaining more attention in recent years. Here, we report the synthesis and application of a hybrid collagen biomaterial with an incorporated ZnO–curcumin (ZnO@Cur) nanocomposite, where the collagen matrix is stabilized using chemically modified TSP (Scheme 1). Curcumin is a natural phenol found in turmeric and it is an active ingredient responsible for its yellow color. It is well known for its antimicrobial, antioxidant, anticancer, anti-inflammatory and wound healing properties. The topical application of curcumin appears to alter the expression of various growth factors, enzymes, MMPs and interleukins and thereby help in faster healing. The low bioavailability of curcumin limits its usage in biomedical engineering and it can be overcome by preparing them in nanoformulations.[18,19] We prepared a nanoformulation of curcumin by incorporating it into ZnO nanoparticles (ZnO@Cur) to overcome its poor bioavailability. Zinc is a major cofactor for the activation of many matrix metalloproteinases (MMPs) involved in the wound healing process. Zinc dependent MMPs help in keratinocyte movement, re-epithelialization, and proliferation of endothelial progenitor cells thereby increasing the angiogenesis.[20,21] Zinc also helps in regulating cellular antioxidants such as glutathione for overall control of redox signaling processes.[22] The prepared hybrid scaffold was characterized for its physical, chemical and biocompatibility properties using various spectroscopic and cytotoxicity analyses. Animal trials along with various histopathological analyses were carried out to ascertain the efficacy of the prepared hybrid scaffold towards scarless burn wound healing.

Materials and methods

Materials

Cowhide trimmings were collected from the local tannery at the Central Leather Research Institute, Chennai. Tamarind seeds were purchased from the local market, Chennai. Collagenase, curcumin, sodium metaperiodate and Pluronics were procured from Sigma-Aldrich, India. Zinc acetate dihydrate, hexane and methanol were purchased from SRL Chemicals, India. Other chemicals used in this study were of analytical grade.

Extraction of the tamarind seed polysaccharide

Tamarind seeds were washed well with tap water to remove tamarind pulp completely from the seeds. The seeds were dried under sunlight and ground to a fine powder using a mill. The seed powder was mixed with methanol : hexane (1 : 1) solution and kept at 50 °C for 1 h to remove the fat and other solvent soluble matter. The solvent mixture was removed and the powder was dried at 30 °C. Distilled water was added to the dried seed powder in a ratio of 1 : 10 and kept at 100 °C for 30 min. Then the heating was stopped and the obtained viscous solution was transferred to an overhead three blade stirrer. The stirring was continued overnight at 30 °C. The viscous solution was centrifuged and the supernatant was collected. The polysaccharide in the supernatant was precipitated by adding methanol to the supernatant in a ratio of 1 : 2. The precipitated polysaccharide was collected by filtration and dried using lyophilization. The lyophilized polysaccharide was ground using a mortar and pestle and stored at 30 °C for further experiments. The extracted polysaccharide was termed tamarind seed polysaccharide (TSP).[23]

Oxidation of TSP

5 g of TSP was dissolved in 450 ml distilled water at 80 °C and 2.5 g $NaIO_4$ dissolved in 50 ml of distilled water was added to the polysaccharide solution. The solution was stirred under dark conditions overnight at 30 °C for 6 h. 10% (v/v) ethylene glycol was added to the polysaccharide solution and stirred for 30 min to quench the reaction. The solution was dialyzed against distilled water for 5 days to remove the unreacted $NaIO_4$. Silver nitrate was used as an indicator to check the release of $NaIO_4$ in distilled water. The oxidized TSP (OTSP) was stored in the solution form at 4 °C for future use. Solid state NMR analysis was carried out for the powder samples of TSP and OTSP. The samples were packed in a cylindrical silicon nitride rotor, and retained with Vespel end caps. The solid-state ^{13}C nuclear magnetic resonance (NMR) spectrum was recorded at 100 MHz using a Bruker 400 MHz solid state NMR spectroscope. TSP and OTSP were also analyzed using a FT-IR spectrometer

(Jasco 4700). The powder samples were ground with KBr using a mortar and compressed into pellets. The pellets were analyzed in the range of 400–4000 cm^{-1} with 2 cm^{-1} resolution.

Synthesis and characterization of the ZnO@Cur nanocomposite

For the synthesis of ZnO nanoparticles, 2 g of zinc acetate dihydrate dissolved in 100 ml distilled water was added to the pH adjusted (pH 10.0) 2% Pluronics solution. The solution was kept under continuous stirring for 30 min at 30 °C and transferred to an oil bath stirrer and refluxed at 130 °C for 8 h. After 8 h of stirring, the solution was allowed to cool to 30 °C and centrifuged at 15 000 rpm to collect the nanoparticles. The precipitate was washed with water three times and dried at 50 °C. Curcumin was loaded to the synthesized ZnO nanoparticles by using the following method. 0.2 g curcumin was dissolved in 50 ml ethanol and it was slowly added to 2 g of ZnO nanoparticles dispersed in 150 ml of ethanol. The solution was kept under stirring for 24 h at 30 °C. After 24 h, the solution was centrifuged and the precipitate was washed twice with water and it was dried using a lyophilizer. The amount of curcumin loaded in the ZnO@Cur nanocomposite was evaluated using UV-visible spectrophotometric analysis (Shimadzu UV1800).

The crystal structure of the prepared ZnO nanoparticle was analyzed using X-ray diffraction (Rigaku miniflex II, Desktop model with a CuKα radiation source, λ = 0.15405 nm). The measurement was carried out at a goniometer speed of 2° min^{-1} in the span of 10 to 80°. The obtained diffraction data were analyzed using JCPDS to confirm its structure. For high resolution scanning electron microscopic (HRSEM) analysis, 1 mg of the ZnO@Cur nanocomposite was dispersed in 1 ml of HPLC grade ethanol using ultra probe sonication at 50% power for 5 min. 20 μl of the dispersed nanoparticles was coated over aluminum foil and ethanol was allowed to evaporate at 30 °C. The aluminum foil with nanoparticles was coated with gold using a sputtering unit and used for HRSEM analysis (FEI Quanta FEG 200). For high-resolution transmission electron microscopic (HRTEM) analysis, 20 μl of the same sample prepared for HRSEM analysis was coated over the copper grid and allowed for ethanol evaporation at 30 °C. The particle size of the prepared nanoparticles was analyzed using a Microtrac wave-II particle size analyzer. For the analysis the particles were dispersed in water using probe sonication and a clear solution was used for the analysis. The images were taken at different magnifications and the lattice space was also calculated. UV-visible and fluorescence spectroscopy of curcumin and the ZnO@Cur nanocomposite was carried out to find out the spectral changes in the curcumin after complex formation with ZnO. FT-IR spectroscopy of ZnO, curcumin and the ZnO@Cur nanocomposite was also carried out.

Preparation of collagen

Collagen was prepared from the cowhide trimmings collected from the pilot tannery at CLRI, Chennai. The collected trimming pieces were limed and delimed using conventional leather processing to remove hair, proteoglycan and fat. The delimed trimming pieces were soaked in 100% methanol for 30 min for partial dehydration. The pieces were then dried using a lyophilizer and stored for future use. The dried delimed pieces were solubilized to a final concentration of 10 mg ml^{-1} using pre-chilled 0.5 M acetic acid at 4 °C for 2 h followed by grinding using a mixer. The solubilized collagen was dialyzed against distilled water at 4 °C for three days with two water changes per day.

Hybrid scaffold preparation and characterization

Dialyzed collagen at 10 mg ml^{-1} concentration was used for the hybrid scaffold preparation. To the collagen solution, 5% (w/w) of OTSP was added as a cross-linking agent and stirred at 4 °C for 15 min. Then, 2 and 5% (w/w) of the ZnO@Cur nanocomposite were added to the collagen solution and stirred at 4 °C for another 30 min. The solution was transferred to a mold and kept at −40 °C for 2 h. The frozen samples were lyophilized for 24 h to form 3D hybrid scaffolds. 5% (w/w) of ZnO and curcumin were added separately to the collagen with OTSP to prepare Coll/OTSP/ZnO 5% and Coll/OTSP/Cur 5% scaffolds. Native collagen solution without OTSP and the ZnO@Cur nanocomposite was also lyophilized to prepare native collagen scaffolds. The changes in the functional groups of collagen were analyzed using FT-IR spectroscopic analysis (Jasco, 4700). The samples were ground with KBr using a mortar and compressed into pellets. The pellets were analyzed in the range of 400–4000 cm^{-1} with 2 cm^{-1} resolution.

CD-spectroscopic analysis of the collagen and hybrid collagen solution was carried out to understand the changes in the triple helical structure of the collagen by the addition of the OTSP and the ZnO@Cur nanocomposite using a Jasco J-815 CD spectropolarimeter. The native and hybrid collagen solution was diluted to 3 μM concentration using 0.2 M sodium acetate buffer and used for the analysis. The CD spectra of the samples were recorded from 190–260 nm under a nitrogen atmosphere.

The degree of cross-linking was determined by measuring the percentage of free amino groups in native and hybrid collagen scaffolds using ninhydrin assay. In this assay, 5 mg of native and hybrid collagen scaffolds were placed in vials separately containing 2 ml distilled water and 1 ml 2% ninhydrin solution in each vial. The vials were kept in a water bath at 100 °C for 20 min and then cooled to 30 °C. The solution was diluted with 10 ml of 50% isopropanol and the absorbance at 570 nm (Abs_{570}) was measured using a UV-visible spectrophotometer. A standard curve was prepared using known concentrations of glycine.[24] The degree of cross-linking was calculated using the eqn (1) as below.

$$\text{Degree of crosslinking} = \frac{\text{Amino}_0 - \text{Amino}_c}{\text{Amino}_0} \times 100 \qquad (1)$$

where $Amino_0$ is the free NH_2 concentration in the native collagen scaffold and $Amino_c$ is the free NH_2 concentration in the hybrid collagen scaffold.

SEM (Phenom Pro) analysis of the cross-section of native and hybrid collagen scaffolds was performed to examine the morphology and porosity of the scaffolds. The samples were

sputter coated with gold for 30 s and used for the analysis. The images were taken at different magnifications. The porosity and pore size distribution of the native and hybrid collagen scaffolds were analyzed using a PMI, HCFP-1100AE porosimeter. The gas permeability of the scaffolds was measured at 30 °C at a gas pressure of 3 psi. A sample with 2 cm diameter was used for the analysis. The pore size distribution was calculated using the flow rate of the liquid through scaffolds at a given pressure.

The thermal stability of the native and hybrid collagen scaffolds was analyzed using a differential scanning calorimeter (DSC, NETZSCH, DSC 204) at a uniform heating rate of 1 °C min^{-1} with a nitrogen flow of 50 ml min^{-1}. In all experiments, 3 mg of wet samples were used for DSC analysis. The viscosity of the native and hybrid collagen solutions was measured using a viscometer (Brookfield, Dv2T) with a temperature regulator (Brookfield, TC-150) at different temperatures (25 to 40 °C). In all the experiments, 6 ml of solution was used for the analysis.

The swelling property of the scaffolds was studied by immersing scaffolds ($1 \times 1 \times 0.5$ cm^3 size) with a known weight in the phosphate buffer saline (PBS) solution. The initial weight of the scaffolds (W_0) was noted and then the scaffold samples were immersed in a vial containing 10 ml of PBS (pH 7.4). The samples were taken out from the vials at specific intervals and the swollen weight of the scaffolds (W_t) was noted after surface bound PBS was removed using absorbent paper. The swelling percentage of the samples was calculated using eqn (2) as follows:

$$\text{Swelling } (\%) = \frac{W_t - W_0}{W_0} \times 100 \quad (2)$$

The enzymatic stability of the scaffolds was studied by incubating them with a known concentration of collagenase solution at physiological pH (pH 7.4). The mass loss of the samples as a function of time of exposure to collagenase was investigated. The dried scaffold sample was weighed (W_i) and immersed in PBS (pH 7.4) to attain a swollen stage. The swollen samples were placed in 15 ml of PBS containing 0.6 μg ml^{-1} collagenase and maintained at 37 °C. At specific intervals, the samples were removed, dried using a lyophilizer and weighed (W_d). The percentage of degradation was calculated using eqn (3) as below.

$$\text{Degradation } (\%) = \frac{W_i - W_d}{W_i} \times 100 \quad (3)$$

The antioxidant properties of the prepared scaffolds were assessed by 2,2-diphenyl-1-picrylhydrazyl (DPPH) assay. 5 mg of the native and hybrid collagen scaffolds were added to 2 ml of 100 μm DPPH solution in methanol. The reaction mixture was incubated in the dark for 30 min and the absorbance was measured at 517 nm.[25] DPPH alone was used as the blank. The DPPH scavenging was calculated using eqn (4) as shown below:

$$\text{DPPH scavenging } (\%) = \frac{A_b - A_s}{A_b} \times 100 \quad (4)$$

where A_b is the absorbance of the blank and A_s is the absorbance of the sample.

Hemocompatibility of the hybrid scaffold

The hemocompatibility of the native and hybrid collagen scaffolds was analyzed using platelet adhesion and hemolytic assay. For the platelet adhesion assay, whole blood was collected and centrifuged at 3000 rpm for 20 min to obtain platelet rich plasma (PRP). The scaffolds were equilibrated with PBS for 30 min at 37 °C. Then the scaffolds were incubated with PRP for 30 min and washed with PBS to remove unattached platelets. The scaffolds with attached platelets were fixed with 2.5% (v/v) glutaraldehyde and observed under a SEM. For hemolytic assay, ethylenediaminetetraacetic acid (EDTA) treated anti-coagulated blood was collected from healthy volunteer donors. The collected blood sample was centrifuged at 1200 rpm for 10 min to pellet RBCs. The collected RBCs were washed with phosphate buffer saline (PBS) twice and centrifuged again. Finally, the RBCs were suspended in PBS and used for the analysis. For the analysis, 50 μl of the suspended RBCs was mixed with 950 μl of PBS. To this solution, 5 mg of native and hybrid collagen samples were added separately. The samples were incubated in the dark at 37 °C for 1 h and then centrifuged at 1200 rpm for 10 min. The absorbance of the centrifuged solution was read at 540 nm using a UV-visible spectrophotometer (Shimadzu UV1800). In this analysis, 50 μl of RBCs mixed with 950 μl of distilled water was used as the positive control and 50 μl of RBCs mixed with 950 μl of PBS was used as the negative control.[26,27] The hemolytic activity was calculated using the following eqn (5).

$$\text{Hemolysis } (\%) = \frac{(\text{OD of sample} - \text{OD of negative control})}{\text{OD of positive control} - \text{OD of negative control}} \times 100 \quad (5)$$

In vitro and *in vivo* analysis of the scaffolds

3-(4,5-Dimethylthiazol-2-yl)-2,5-diphenyltetrazolium bromide (MTT) assay was performed using human epidermal keratinocyte cells to check the cytocompatibility of the prepared native and hybrid collagen scaffolds. The scaffolds were cut into circular pieces and sterilized by UV irradiation. The samples were placed in a 6-well plate and seeded with 1×10^4 cells followed by incubation in Dulbecco's modified Eagle's medium at 37 °C under 5% CO_2. After 24, 48 and 72 h of incubation, 100 μl of MTT (5 mg ml^{-1}) was added to each well and the plate was incubated at 37 °C for 4 h. Dimethyl sulfoxide was added to all the wells to dissolve the formed formazan completely. The plates were read using a multi plate reader (PerkinElmer) at 570 nm. Furthermore, the cell viability was analyzed by live–dead cell staining using calcein AM. After 48 h of incubation of the cells as prepared above, the medium was discarded and 0.5 ml of PBS containing 1 μM calcein AM and 1.5 μM propidium iodine was added to each well, followed by incubation for another 30 min. Subsequently, the cells were observed using a fluorescence microscope (Leica) and the images of the cells were captured.

32 healthy male albino rats weighing 200–220 g were used for the *in vivo* burn wound healing experiments. All animal protocols were explained to the ethical Committee of the Council for Scientific and Industrial Research-Central Leather Research Institute (CSIR-CLRI) and they were approved for further experiments (Reg. No. 466/01a/Committee for the Purpose of Control and Supervision of Experiments on Animals). Animals were bought from the King Institute of Preventive Medicine and Research, Chennai, and they were kept in polypropylene cages at 24 ± 2 °C. The animals were fed with standard balanced food and drinking water. After 7 days of procurement, the animals were orally administered with a deworming agent (Albendazole). The animals were divided into five groups namely open wound (OW), native collagen scaffold (Coll) treated, collagen–ZnO scaffold treated (Coll/OTSP/ZnO 5%), collagen–curcumin scaffold treated (Coll/OTSP/Cur 5%) and hybrid collagen scaffold treated (Coll/OTSP/ZnO@Cur 5%) groups. After the rats were anesthetized with diethylether, the hair on the dorsal side was shaved using a shaving blade before a day of burn wound creation to avoid over stress on the skin. Burn wounds were created using a red hot metal template (1.5 cm diameter) held at 90° on the shaved dorsal side of the rat for 20 s. The thermal images of the rat before and after burn wound creation were taken using an IR-camera (FLIR, E60). After 24 h of burn wound creation, the dead tissue was excised and dressed with respective materials according to their grouping (native and hybrid collagen scaffolds). The respective scaffolds were placed over the wound and dressed with 3M micropore surgical adhesive tape to keep the scaffolds on the wound site. The scaffolds were changed every three days. However, if the animal removed the bandage before the completion of three days, the dressing was re-done again. The open wound group animals were dressed with sterile gauze alone. Granulation tissues were collected from all the animals on 7th and 14th day of the experiment. After healing, the animals were kept for another 30 days to allow skin maturation and the regenerated skin was collected by excision. The collected granulation tissue and the regenerated skin were stored in 10% formalin solution and used for histological and immunohistochemical analyses. The tissue samples were embedded in paraffin and cut into 4 ± 1 μm thick frozen sections using a cryostat microtome. The micro-sectioned tissue samples were stained with Hematoxylin and Eosin (H&E) and Masson's trichrome to observe the structures and collagen deposition in the newly formed skin. The slides were observed under a ZEISS Scope A1 and the images were taken. Furthermore, the wound area was calculated by mapping the wound at different days on a tracing sheet. The digital images of the burn wound were also taken on different days to visualize the wound healing pattern. All the animals were euthanized after the completion of the experiments according to the ethical guidelines using a CO_2 chamber. The scar elevation index (SEI) is the ratio between the hypertrophied dermis and the underlying dermis of the wounded skin to the normal dermis of the unwounded skin.[28] Typically a rabbit ear model of hypertrophic scarring is used to assess the scar formation quantitatively. The growth of new tissue (including epidermis and dermis) over the cartilage base is measured to quantify the SEI. Although it is not possible to quantitatively measure the SEI in rat models due to the absence of the cartilage base, we employed a relative semi-quantitative measurement in this study. The SEI value for the normal skin is 1 and the increase in the SEI value is directly related to the increase in the scar formation in the newly regenerated skin.

For immunostaining analysis, microsections of the fully regenerated skin were placed on poly L-lysine coated slides and deparaffinized using xylene. It was dehydrated using graded ethanol solution and boiled in citrate buffer for 30 min to retrieve the epitopes needed for the CD31 and TGF-β3 detection. After blocking the endogenous peroxidase activity, the tissue samples were covered with primary antibodies for 60 min. The sections were decolorized and counterstained with hematoxylin and used for the microscopic analysis.

Results and discussion

Characterization of the polysaccharide

Solid state NMR analysis of OTSP confirmed the formation of the aldehyde group (Fig. S1, ESI†). The ^{13}C NMR spectra show five well-resolved signals for both TSP and OTSP, which match well with previously reported data.[29] An additional peak at 173 ppm observed for OTSP is attributed to the carbonyl carbon of the aldehyde group.[30] The changes in the functional groups were further confirmed by FT-IR spectroscopic analysis. The FT-IR spectra of TSP and OTSP are shown in Fig. S2 (ESI†). The wide band observed around 3400 cm^{-1} is attributed to the stretching of the –OH groups present in the TSP and OTSP. The peak at 2925 cm^{-1} may be due to the asymmetric stretching of C–H and the peak at 1030 cm^{-1} is attributed to the C–O–C stretching mode. The peak at 1645 cm^{-1} may be due to the –CH–OH stretching vibration.[31,32] The low intensity C═O stretching band found at 1730 cm^{-1} (Fig. S2b, ESI†) confirmed the presence of aldehyde groups in OTSP.[30]

Characterization of ZnO nanoparticles and the ZnO@Cur nanocomposite

XRD analysis of the ZnO nanoparticles shows major diffraction peaks at 31.5°, 34.3°, 36.2°, 47.3°, 56.6°, 62.8°, 66.3°, 67.8°, 69.1° and 77.1° corresponding to the (100), (002), (101), (102), (110), (103), (200), (112), (201) and (004) lattice planes, respectively (Fig. 1a). The *d*-spacing values of the (100), (002) and (101) planes are found to be 0.28, 0.26 and 0.24 nm, respectively. The XRD result is in agreement with the hexagonal wurtzite structure of ZnO (JCPDS no. 36-1451).[33] No additional peaks related to any other impurities were found in the sample thus revealing the purity of ZnO nanoparticles. The HRSEM and TEM analyses show flower-like microstructural arrangements in the as-synthesized ZnO (Fig. S3a and b, ESI†). The high magnification HRSEM image clearly shows an individual flower with 500 nm size encompassing nanopetals (Fig. 1b). The size of the nano petals varies between 15 and 70 nm from the upper to lower portion, respectively,

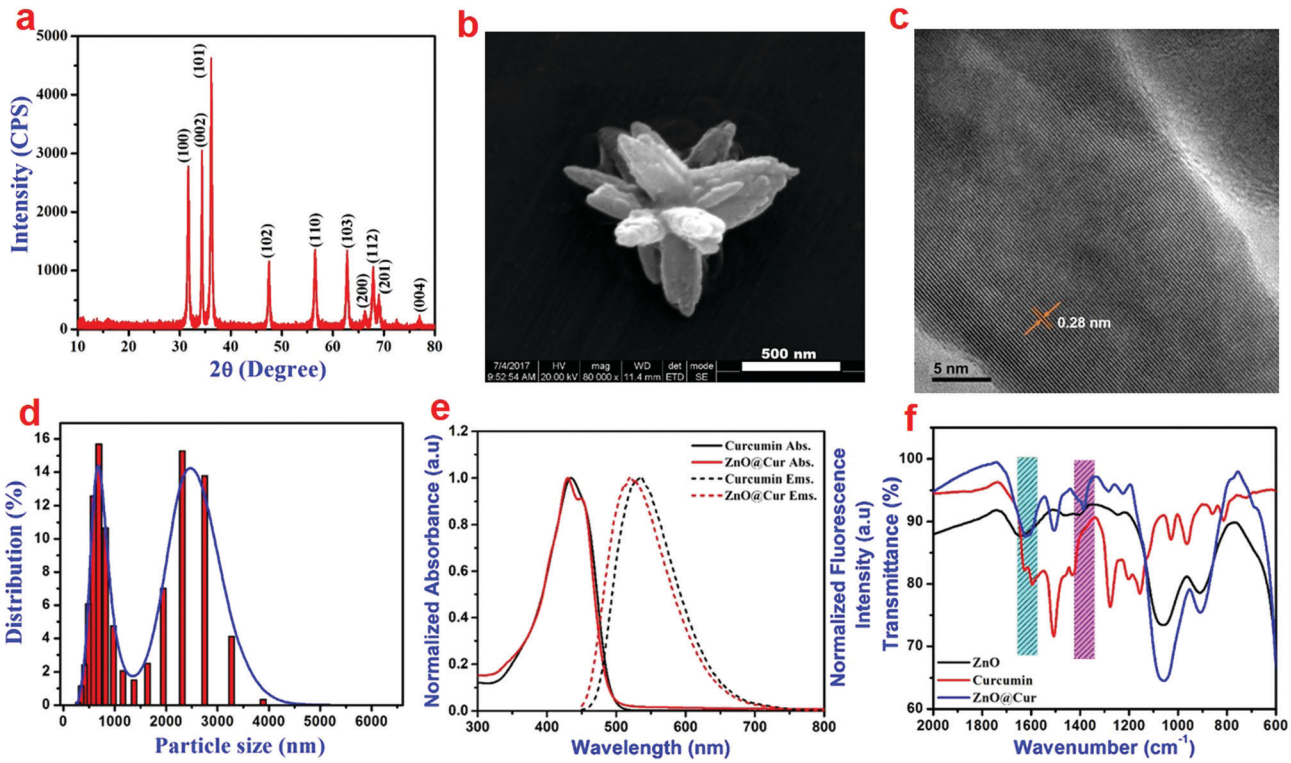

Fig. 1 (a) XRD, (b) HRSEM, (c) HRTEM, (d) particle size distribution of the prepared ZnO nanoparticles; (e) absorption and emission spectra of curcumin and the ZnO@Cur nanocomposite; (f) FT-IR spectra of the ZnO nanoparticles, curcumin and the ZnO@Cur nanocomposite.

as seen in the HRTEM image (Fig. S3c, ESI†). The calculated *d*-spacing value is found to be 0.28 nm from the lattice arrangements of the nanoparticles as observed from the higher magnification HRTEM image (Fig. 1c). It is in good agreement with the *d*-spacing value calculated from the XRD results corresponding to the (100) plane of ZnO. Furthermore, the DLS analysis reveals a broad range of particle distribution (Fig. 1d), where most of the particles are present in the range of 300–600 nm and very few particles are in the range of 1–4 μ.

The absorption and emission spectra of the prepared ZnO@Cur nanocomposite was compared with those of curcumin alone to verify the interaction between ZnO and curcumin (Fig. 1d). The UV-visible spectra of curcumin show an absorption peak at 430 nm due to π–π* electron transitions, which corresponds to the enol form of curcumin. The ZnO@Cur nanocomposite also shows a major absorption peak at 430 nm with an additional shoulder peak at 451 nm. Furthermore, the emission spectra of curcumin and ZnO@Cur were also analyzed to confirm the interaction. Curcumin shows the maximum emission at 533 nm, whereas the emission of the ZnO@Cur nanocomposite is blue-shifted to 520 nm. The appearance of the shoulder peak in the absorption spectrum and the blue-shift in the emission spectrum of the ZnO@Cur nanocomposite could be attributed to the formation of a ligand-to-metal charge-transfer complex.[34]

The functional groups in the prepared ZnO nanoparticles, curcumin and the ZnO@Cur nanocomposite were analyzed using FT-IR spectroscopy (Fig. S4, ESI† and Fig. 1f). The FT-IR spectra of the prepared ZnO show peaks at 1060 and 908 cm^{-1}, which could be attributed to the C–O stretching vibration and C═H bending of the Pluronics on the surface of the nanoparticles. The characteristic absorption bands of curcumin corresponding to the stretching and bending vibrations of phenolic O–H are observed at 3510 and 1380 cm^{-1}, respectively, although the latter appeared as a shoulder peak (Fig. S4, ESI† and Fig. 1f). Other peaks at 1630, 1600, 1505, 1435 and 1275 cm^{-1} can be assigned to the stretching vibrations of the benzene ring, C═O, C–C, C–H bending vibration and aromatic C–O stretching vibration, respectively. The ZnO@Cur nanocomposite shows a clear peak at 1382 cm^{-1}, which could be due to the bending vibration of phenolic O–H present in curcumin molecules. The peak at 1630 cm^{-1} disappeared and the C═O peak at 1600 cm^{-1} is shifted to 1620 cm^{-1} in the ZnO@Cur nanocomposite, which could be due to the charge-transfer interaction of curcumin with ZnO.[35]

Characterization of the scaffolds

The FT-IR spectra of the native and hybrid collagen scaffolds are shown in Fig. S5 and S6 (ESI†). The FT-IR spectrum of the native collagen scaffold shows all characteristic absorption bands of amide I, amide II and amide III at 1660 (C═O stretching), 1550 (N–H bending and C–N stretching) and 1240 cm^{-1} (C–N stretching and N–H bending), respectively.[36] It is expected that the interaction between OTSP and collagen will lead to the appearance of a characteristic band around 1630 cm^{-1} due to the formation of the imine (C═N) linkage. However, here, the collagen molecule also shows its characteristic band for amide I

around 1650 cm^{-1}, and therefore it is difficult to confirm the interaction of OTSP with collagen. Nevertheless, the reaction between the aldehyde and amine group can be confirmed by the reduction in the intensity of the amide III peak at 1240 cm^{-1}.[37] The Amide-I band on the FT-IR spectrum of the hybrid scaffold did not show any shift upon interaction with OTSP, which confirmed the unaltered secondary structure of the collagen.[36] The interaction of the ZnO@Cur nanocomposite with the OTSP stabilized collagen does not further alter the spectral features in the hybrid scaffold.

Furthermore, CD spectroscopy for the native and hybrid collagen solutions was carried out to understand the effect of the OTSP and the ZnO@Cur nanocomposite on the triple helical structure of the collagen (Fig. S7, ESI†). The results show that there is no change in the positive peak of the collagen molecule appearing at 220 nm. The unchanged position of the positive peak in the CD spectra reflects that the triple helical nature of the collagen molecule is not altered in the hybrid collagen scaffold. It is interesting to note that the intensity of the negative peak at 197 nm is increased in the hybrid collagen solution. The increased intensity of the negative peak may be due to the covalent interaction of OTSP with the collagen molecules.[38] The crossover point of the native collagen (210 nm) did not change after the addition of the OTSP and the ZnO@Cur nanocomposite. Since both FT-IR and CD spectroscopic analyses did not show convincing evidence for the interaction between collagen and OTSP, we performed ninhydrin assay to estimate free amino groups in the native and hybrid collagen scaffolds. The result shows that 73% of the amino groups are cross-linked in the hybrid scaffold, when compared to the amino groups present in the native collagen scaffold. This analysis reveals the potential of the prepared OTSP in cross-linking collagen molecules.

SEM analysis of native and hybrid collagen scaffolds was carried out to view the cross sectional morphology (Fig. 2a–c). The SEM images of both the native and hybrid scaffolds show a

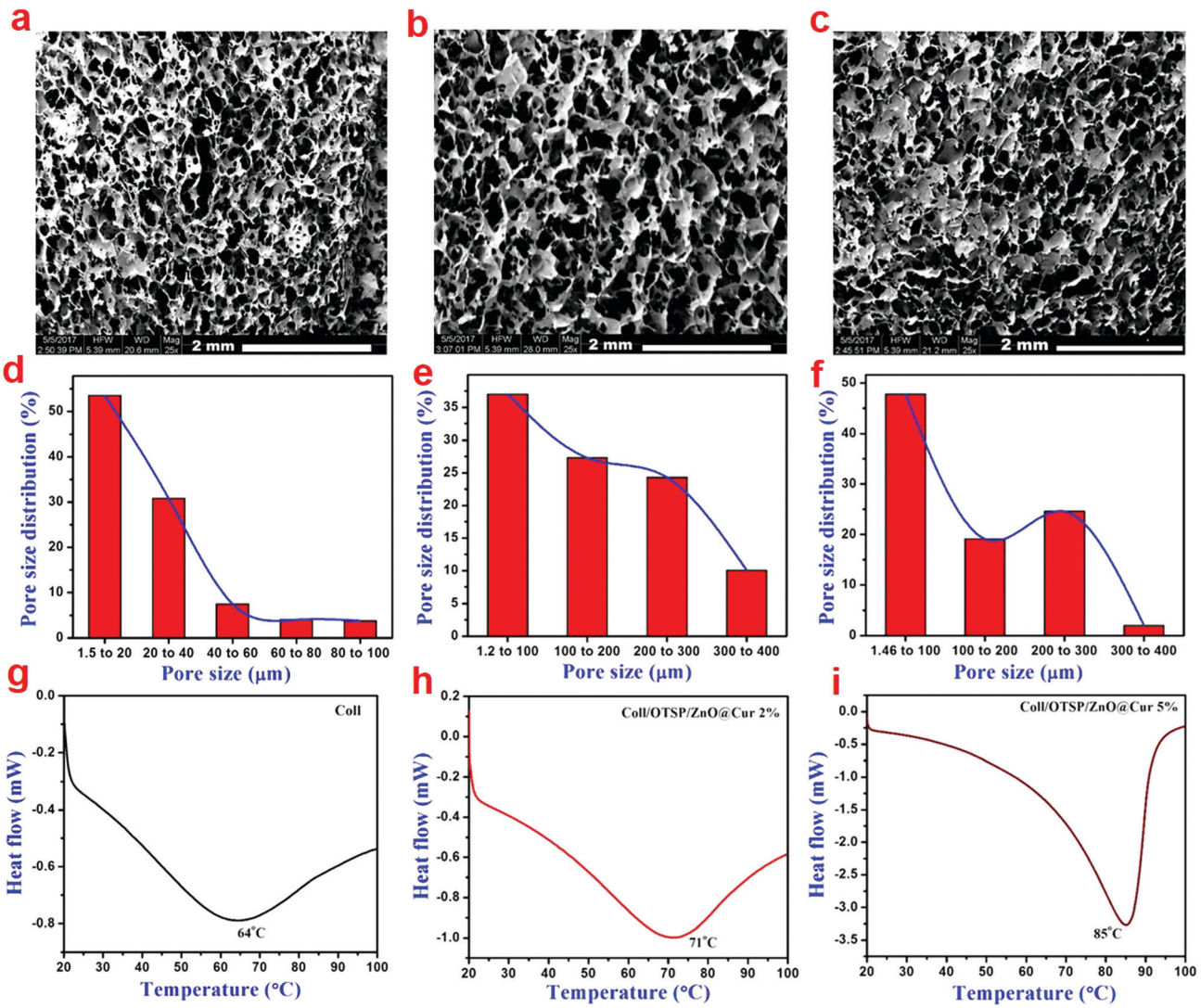

Fig. 2 (a–c) SEM images showing the cross-sectional morphology, (d–f) gas permeability and (g–i) DSC traces of collagen, Coll/OTSP/ZnO@Cur 2% and Coll/OTSP/ZnO@Cur 5% scaffolds, respectively.

well interconnected porous structure. From the SEM analysis, it could be observed that the addition of OTSP and ZnO@Cur to collagen did not affect the porous nature of the scaffolds. Furthermore, the pore size distribution was analysed using a porosimetric technique to quantify the pore characteristics of the native and hybrid collagen scaffolds. The porosimetry results demonstrate that the pore size of the hybrid scaffolds is increased when compared to that of the native collagen scaffold (Fig. 2d–f). The pore size distribution of the native collagen scaffold is found to be in the range of 1.5 to 100 μ, where the hybrid scaffolds show a pore size distribution in the range of 1.5 to 400 μ. The larger pore size may be due to the OTSP induced crosslinking of the collagen molecules.

Differential scanning calorimetric (DSC) analysis was carried out to understand the effect of the OTSP and the ZnO@Cur nanocomposite on the thermal stability of collagen. The shrinkage temperature of the native collagen was found to be around 64 °C (Fig. 2g) matching well with previously reported data.[39] The addition of the OTSP and the ZnO@Cur nanocomposite increases the shrinkage temperature of the hybrid scaffolds to 71 and 85 °C for 2 and 5 wt% of the ZnO@Cur nanocomposite, respectively (Fig. 2h and i). From the results, it could be observed that the ZnO@Cur nanocomposite also plays a role in increasing the shrinkage temperature of the collagen apart from OTSP. Curcumin is a naturally occurring phenolic molecule with more hydroxyl groups. Hence, the ZnO@Cur nanocomposite is expected to interact with collagen molecules electrostatically or through hydrogen bonds an in the case of plant polyphenol based stabilization of collagen during leather making.[40] Furthermore, the viscosity of the native and hybrid collagen solutions was analyzed as a function of temperature to understand the thermal stability of the scaffolds. It is seen that the viscosity of the collagen solution is increased with the addition of the OTSP and the ZnO@Cur nanocomposite (Fig. S8a, ESI†). The increase in the viscosity may be due to the interaction of the OTSP and the ZnO@Cur nanocomposite with the collagen. We obtained the melting temperature from the second derivative of the change in viscosity with respect to temperature. As can be seen, the melting temperature of the native collagen solution is around 36 °C, which is closer to the reported melting point (~37 °C) of the native collagen. However the melting temperature of the hybrid collagen solutions is around 43 °C indicating the increased thermal stability of collagen after interaction with OTSP.

The swelling ability of the scaffolds would help in the absorption of more exudates from the burn wounds and maintaining the moisture environment in the wound bed. The swelling ratio of the native and hybrid collagen scaffolds is shown in Fig. S8b (ESI†). As can be observed, the native and hybrid collagen scaffolds attained maximum swelling within 1 h. The hybrid scaffold shows a higher swelling (~2300%) compared to the native collagen scaffold (1200%). The enzymatic degradation stability of the scaffolds was evaluated against collagenase. It is seen that more than 70% of the native collagen scaffold (Fig. S8c, ESI†) is degraded within 24 h of incubation and it is completely degraded within 48 h. However the hybrid scaffold shows enhanced enzyme stability with only about 50% degradation even after 72 h of incubation. Furthermore, it is interesting to note that the addition of the ZnO@Cur nanocomposite (2 and 5 wt%) did not alter both the swelling and enzymatic stability of the hybrid scaffolds.

Oxidative stress may lead to metabolic dysfunctions, loss of cell integrity and hindrance in enzyme activities. During burn wound healing, the body produces more reactive oxygen species (ROS), which would lead to slow healing. A common approach to reduce the ROS formation is the use of suitable antioxidants during the fabrication of biomaterials. The free radical scavenging activity of the native collagen and hybrid scaffolds was analyzed using DPPH assay and the results are shown in Fig. S8d (ESI†). It is seen that the native collagen scaffold has 35% antioxidant activity and it has been proposed that the Gly-Pro sequence and methionine present in the collagen molecule a play significant role in the free radical scavenging activity.[41] On the other hand, the hybrid scaffolds demonstrate 62 and 71% antioxidant activity after the addition of the 2 and 5 wt% ZnO@Cur nanocomposite, respectively. The enhanced antioxidant activity of the hybrid scaffolds can also help in faster re-epithelialization by neutralizing not only ROS but also bacterial toxins.

Hemocompatibility of the scaffolds

Hemocompatibility, an important property, plays a role in the activation of blood cells and initiation of the wound healing process. The SEM images of the scaffolds treated with PRP were taken to visualize the response of platelets to native and hybrid scaffolds (Fig. 3a–c). Both native and hybrid scaffolds exhibit good attachment of platelets. Furthermore, we have also observed pseudopodia formation on the attached platelets. Zn in the ZnO@Cur nanocomposite may help in the platelet activation by stimulating protein kinase C and increasing the fibrinogen receptor exposure on the platelet's surface.[27] The hemolytic activity of the native and hybrid collagen scaffolds was also evaluated and it is found to be ~5% for both the scaffolds. It is within the allowable range according to the ASTM F 756-00 standard for materials used in biomedical applications.[42] The digital images of the hemolytic activity are shown in Fig. S9 (ESI†).

In vitro and *in vivo* analysis of the scaffolds

Biocompatibility is a key property of the scaffolds that is intended for biomedical applications. The human epidermal keratinocyte cell line was used to study the cytocompatibility of native and hybrid collagen scaffolds using MTT assay. The hybrid scaffolds show nearly 80% of cell viability after 24 h (Fig. 3d). The cell viability increased significantly as the time of incubation increased. After 72 h of incubation, the hybrid scaffolds exhibited proportionately good cell viability similar to native collagen scaffolds. Furthermore, the calcein-AM stained images, taken after 48 h of incubation period, confirm the attachment and proliferation of keratinocyte cells to the native and hybrid collagen scaffolds (Fig. 3e–g). These results suggest that the prepared hybrid scaffolds are biocompatible and can be used for *in vivo* applications. Furthermore, they also

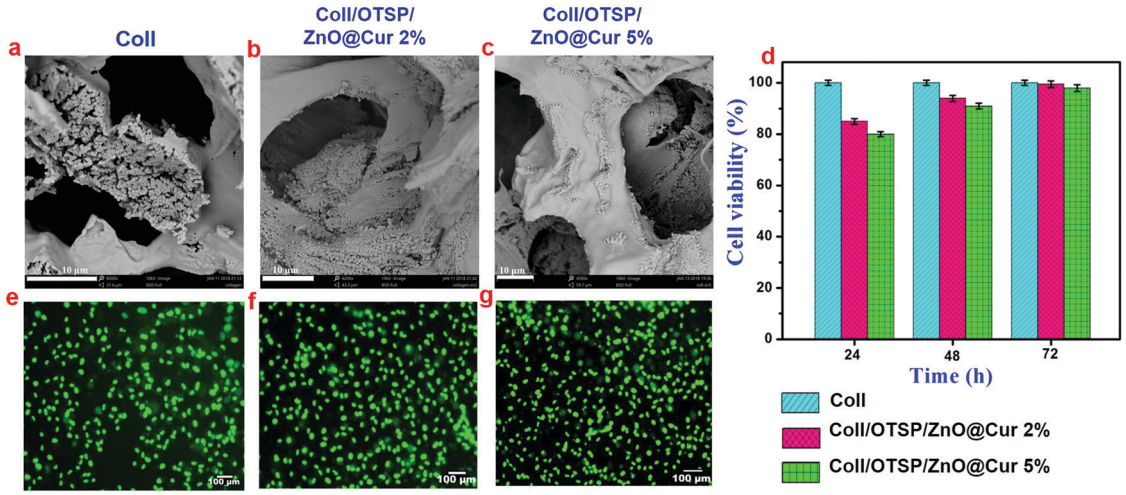

Fig. 3 (a–c) SEM images showing the platelet attachment to the collagen, Coll/OTSP/ZnO@Cur 2% and Coll/OTSP/ZnO@Cur 5% scaffolds, respectively; (d) cell viability of the scaffolds analyzed using MTT assay at 24, 48 and 72 h of cell proliferation; (e–g) human keratinocyte proliferation on the collagen, Coll/OTSP/ZnO@Cur 2% and Coll/OTSP/ZnO@Cur 5% scaffolds, respectively after 48 h of incubation determined using calcein-AM staining.

show that the higher concentration of the ZnO@Cur nanocomposite (5 wt%) did not affect the viability and proliferation of the human keratinocyte cells.

The thermal images of the animals used for *in vivo* applications were taken before and after creating burn injury to confirm the surface temperature. The temperature of the shaved animal before burn wound creation is 36.8 °C and the temperature of the wound area rose to 120 °C after creating the burn wound (Fig. 4a and b). The digital images of the burn wound at different days of treatment are shown in Fig. 4c. It is seen that the hybrid collagen scaffold has led to rapid healing of the burn wound in about 21 days after treatment. However the native collagen, collagen–ZnO, collagen–curcumin scaffold treated and untreated groups did not show complete wound healing even after 21 days of treatment. The wound closure percentage at different days of treatment is shown in Fig. 4d. After 21 days of treatment, the wound closure percentage is found to be 65 and 80% for untreated and native collagen scaffold treated groups, respectively. However it is 82 and 91% for collagen–ZnO (Coll/OTSP/ZnO 5%) and collagen–curcumin (Coll/OTSP/Cur 5%) scaffold treated animal groups, respectively, and the hybrid collagen scaffold treated group displays 100% closure.

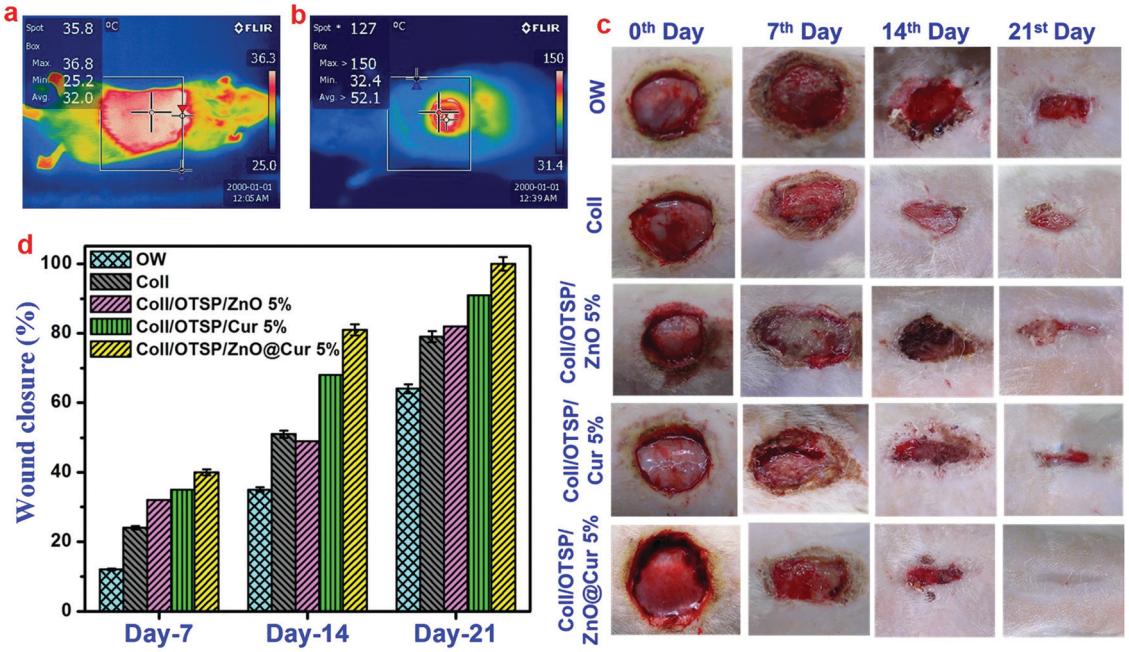

Fig. 4 Thermal images of the shaved rat (a) before and (b) after burn wound creation. The blue color region indicates low temperature and the red color region indicates high temperature, as per the temperature scale shown on the right side of the images; (c) digital images of the wound of different animal groups at different days of treatment; (d) percentage of wound closure of all the animal groups on 7th, 14th and 21st day of healing.

The effect of untreated and treated groups with different scaffolds on inflammation was assessed by CD68 immunohistochemical staining. It is evident that the hybrid scaffold treated group shows a small number of macrophages on the 7th day of healing when compared to the other groups (Fig. 5). In addition, it is interesting to note that the Coll/OTSP/Cur 5% treated group also shows fairly less inflammation compared to Coll/OTSP/ZnO 5% and native collagen treated animal groups. Curcumin is known to regulate different molecular targets such as inflammatory cytokines, growth factors and transcription factors and thereby exhibits anti-inflammatory activity.[43] The open wound, native collagen and Coll/OTSP/ZnO 5% scaffold treated groups show high inflammation even on the 14th day of healing whereas the Coll/OTSP/Cur 5% scaffold treated group shows less inflammation and the hybrid scaffold treated group shows very few macrophages. The increased anti-inflammatory action of the hybrid scaffolds could be due to the increased bioavailability of curcumin in the ZnO@Cur nanocomposite. Reduced inflammatory response is one of the major factors required for fast and scarless healing.[44] Hence, the increased anti-inflammatory activity of the hybrid scaffolds is expected to assist in scarless healing.

The growth and architecture of the skin during different phases of healing was further analyzed using different staining techniques such as H&E and Masson's trichrome. The loss of the epidermal layer, skin appendages and the disorganized collagen layer was observed in the collected eschar tissue after burn wound creation (Fig. S10, ESI†). On the 7th day, the hybrid scaffold treated animals show much less inflammation than the untreated and native collagen scaffold treated groups (Fig. S11, ESI†), which could be due to the anti-inflammatory properties of ZnO and curcumin in the hybrid scaffold. It has been shown through *in vitro* studies that curcumin reduces the inflammation by suppressing the expression of tumor necrosis factor-α (TNF-α) and interleukin-1 (IL-1).[45,46] In addition, new blood vessels are formed and few fibroblast cells are also seen only in the hybrid scaffold treated group, which indicates that the proliferative stage has already begun unlike the other groups. Previous reports on curcumin have proved that it plays a key role during the proliferation stage by increasing the fibroblast production and migration and thereby facilitating wound contraction.[45,47] Furthermore, the Zn^{2+} ions released from ZnO serve as a cofactor for the many enzymes like zinc dependent matrix metalloproteinases, which play a crucial role in keratinocyte migration during the wound repair.[22,48] On the 14th day, keratinized and epidermal layers are formed in the hybrid scaffold treated group unlike untreated and native collagen scaffold treated groups (Fig. S11, ESI†). The presence of the keratinized layer in the hybrid scaffold treated animals indicates that the wound contraction has initiated on the 14th day of healing. Overall, the inflammation phase is adequately controlled in the hybrid collagen scaffold treated group when compared to other groups. As a result of fast re-epithelialization and angiogenesis, hybrid scaffold treated animals show a basic

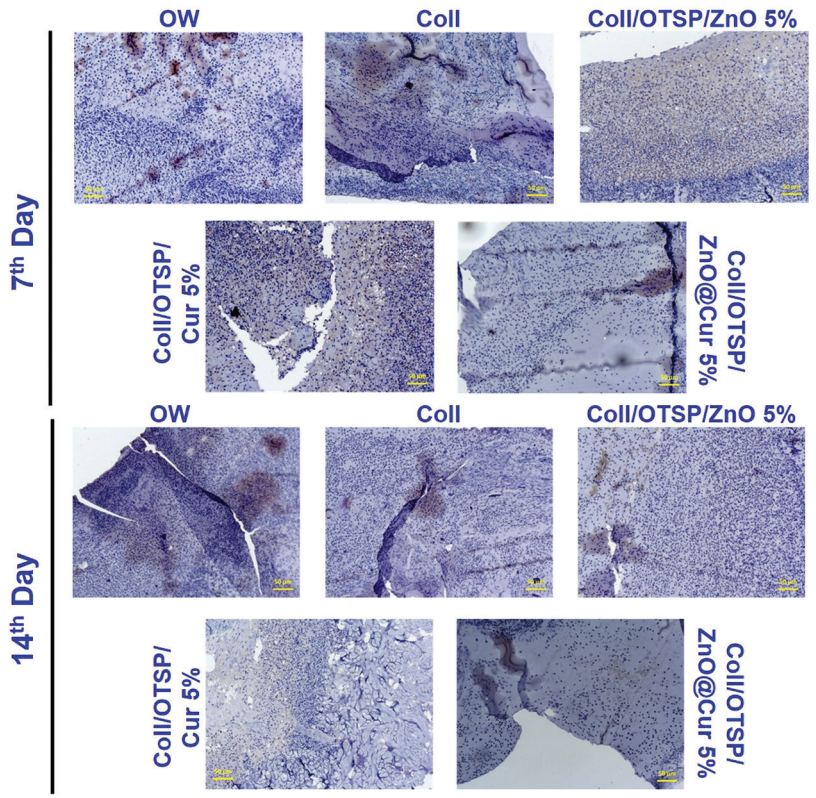

Fig. 5 CD68 immunohistochemical staining of the granulation tissue collected on the 7th and 14th day of treatment from all the animal groups namely open wound, native collagen, Coll/OTSP/ZnO 5%, Coll/OTSP/Cur 5% and hybrid collagen scaffold treated groups (the scale bar is equivalent to 50 μm).

skin structure with developed epidermis, dermis and blood vessels on the 14th day of healing, whereas the native collagen scaffold treated and open wound groups did not show any such development.

After 21 days of healing followed by 30 days of maturation, the whole regenerated skin on the wound area was excised and histological studies were performed. The histological images of the regenerated skin collected from all the groups at a lower magnification show the basic architecture of the skin with all appendages such as the sebaceous gland, hair follicles and blood vessels (Fig. S12, ESI†). However, there is slight variation in the locations of these appendages in the untreated and native collagen scaffold treated groups. As the epidermal layer is thicker and elevated and also dense collagen fibers are present in the wound site of the untreated and native collagen scaffold treated groups, the appendages are present almost in the hypodermis area (Fig. 6 and Fig. S12, ESI†). These features also indicate the scar formation in these groups. On the other hand, the hybrid scaffold treated group shows a perfect skin architecture akin to the unwounded skin (Fig. S12a and d, ESI†). We estimated the thickness of the epidermal layer on the newly regenerated skin of the untreated and native collagen scaffold treated groups from the magnified images of the epidermal area as shown in Fig. 6a and b and it was found to be 82 ± 2 and 86 ± 2 μm (Fig. 6g). However, it was only 30 ± 2 μm (Fig. 6c) for the hybrid scaffold treated group and comparable to the thickness of the unwounded normal skin (22 ± 2 μm). The relative SEI of the newly formed dermis was also measured to evaluate the scar formation semi-quantitatively. From the results (Fig. 6h), we demonstrate that the hybrid scaffold treated animals show negligible scar formation with a relative SEI value of 1.3 ± 0.1. On the other hand, the open wound and native collagen scaffold treated animals show relative SEI values of 2.8 ± 0.1 and 2.5 ± 0.1, respectively.

Masson's trichrome staining was carried out to understand the deposition of collagen during the wound healing phase. As can be seen, there is no collagen deposition on the 7th day of healing in any of the groups (Fig. S11, ESI†). On the 14th day, significant collagen deposition is seen in the hybrid scaffold treated animal group while the open wound and native collagen treated groups do not show any collagen deposition (Fig. S11, ESI†). The fully regenerated skin collected from the hybrid scaffold treated group (Fig. 6f) shows well aligned collagen fibers comparable to the unwounded skin. However, the open wound and native collagen

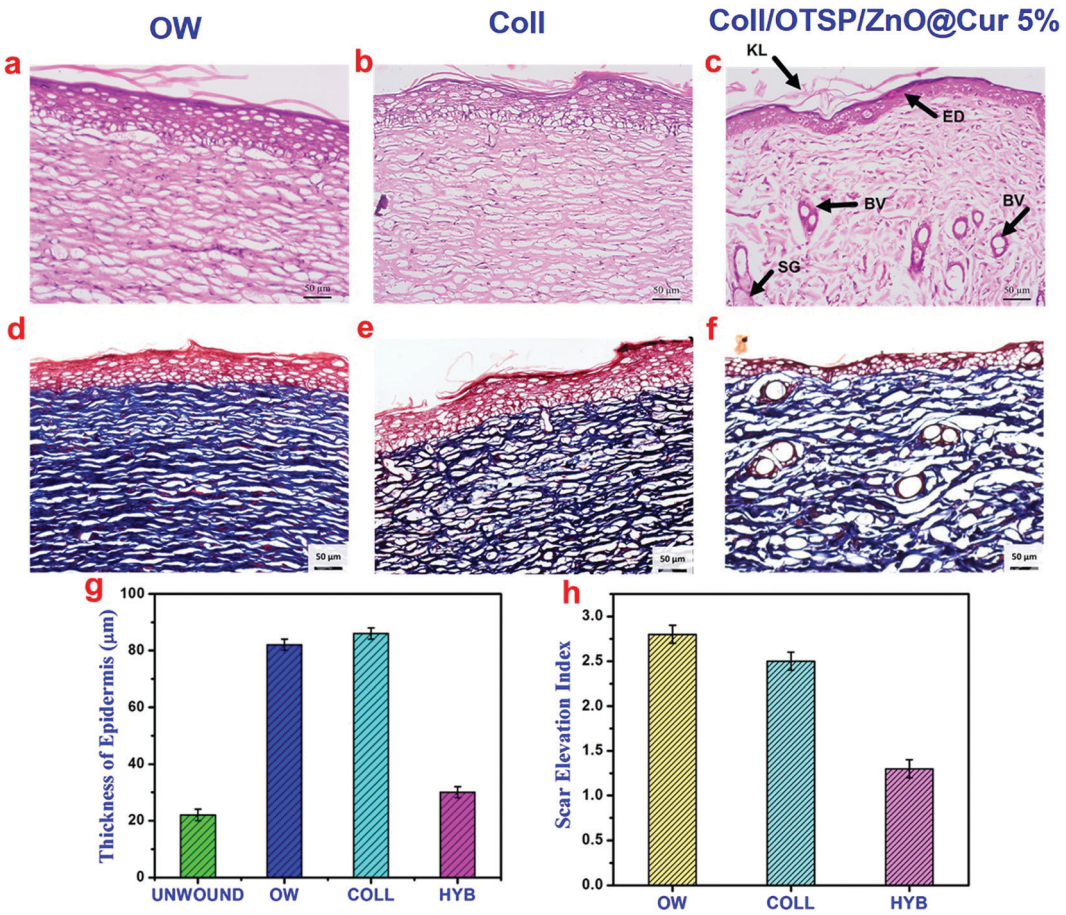

Fig. 6 (a–c) H&E and (d–f) Masson's trichrome staining of the newly regenerated skin collected after 21 days of healing followed by 30 days of maturation from all the animal groups namely open wound, native collagen and hybrid collagen treated groups, respectively. KL stands for the keratinized layer, ED stands for the epidermal layer, SG stands for the sebaceous gland and BV stands for blood vessel in the image; (g) thickness of the epidermis in the unwounded skin and experimental groups; (h) semi-quantitative scar elevation index for all the experimental groups.

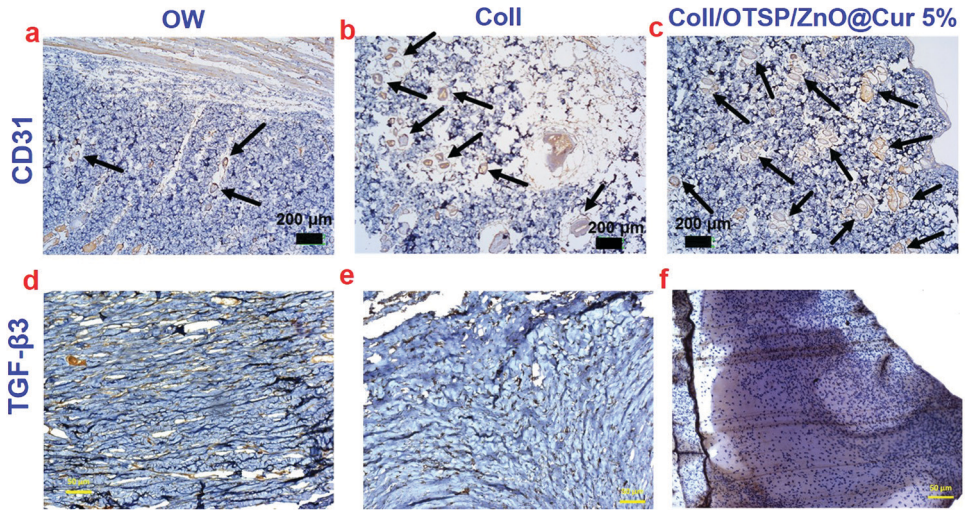

Fig. 7 (a–c) CD31 and (d–f) TGF-β3 immunohistochemistry staining of the newly regenerated skin collected from all the animal groups namely open wound, native collagen and hybrid collagen treated groups, respectively. The arrows in images (a–c) indicate blood vessels.

scaffold treated groups show disordered and thick collagen fiber deposition indicating the scar formation (Fig. 6d and e).

New blood vessels participate in the granulation tissue formation and they carry oxygen and nutrients to the growing tissues. Any defect in the angiogenesis eventually affects further processes and leads to delayed wound healing. CD31 immunochemical staining was performed to ascertain the formation of new blood vessels (Fig. 7a–c). The number of blood vessels in a specific field was counted in all the groups and the results are shown in Fig. S13 (ESI†). The untreated open wound group animals show only 7 ± 2 blood vessels in a specific field. However 19 ± 1 and 34 ± 1 blood vessels are seen in the native collagen and hybrid collagen scaffold (Coll/OTSP/ZnO@Cur 5%) treated groups, respectively. Curcumin is reported to up-regulate the expression of vascular endothelial growth factors and induce new blood vessel formation by increasing the endothelial cell proliferation and preventing their apoptosis.[49] Transforming growth factor-beta (TGF-β) is another major factor that regulates proliferation, cellular differentiation and other functions in cells during the wound healing process. There are three prototypic TGF-β isoforms namely TGF-β1, TGF-β2 and TGF-β3 that are structurally similar cytokines encoded by distinct genes but expressed differently in adult and fetal wound healing. Research on fetal wound healing reveals that the expression of TGF-β3 is increased during scarless wound healing,[50] although the exact mechanism still remains to be understood. TGF-β3 immunochemical staining shows higher expression in the hybrid scaffold treated group compared to that in the native collagen scaffold treated and untreated groups (Fig. 7d–f).

The effect of curcumin and other related phenols on the inhibition of keloid and hypertrophic scar derived fibroblasts has been studied.[51] Zinc oxide based adhesive tape is also reported for its potency in the treatment of scars.[52] However, hitherto no reports are available to show the effect of ZnO and curcumin on the expression of TGF-β3. Here, we have shown that the hybrid scaffold treated group shows enhanced expression of TGF-β3 when compared to the other two groups through immunocytochemistry analysis. This could be due to the combined effect of ZnO and curcumin in combination with collagen in the hybrid scaffold. The TGF-β signaling pathway involves the binding of TGF-β superfamily ligands to a type-II receptor (TβRII), followed by phosphorylation of type-I receptor and receptor-regulated SMAD. It has been shown that TGF-β3 stimulates a sustained phosphorylation of SMAD2/3 in the epidermal cells than in the dermal cells.[53] Such a difference is shown to be due to the differential expression of TβRII during the wound healing process. SARA (SMAD anchor for receptor activation), a zinc double finger FYVE domain containing protein, binds to the MH2 (MAD homology 2) domain of SMAD2/3 and controls the subcellular localization of SMAD during the TGF-β signaling pathway.[54] The FYVE fingers of SARA bind to two Zn ions. Furthermore, it has been shown that Cu and Zn increase the gene expression of TβRII thereby reducing the intestinal injury in *Escherichia coli* LPS-challenged weaned pigs.[55] Therefore, it is proposed that the zinc ions from the ZnO@Cur nanocomposite of our hybrid scaffolds assist in up-regulation of TGF-β3 by increasing the expression of TβRII and possibly SARA. Nevertheless, detailed research is needed to find the mechanism behind the role of zinc ions and curcumin in regulating the expression of TGF-β3.

Conclusions

Here, we have synthesized a polysaccharide based cross-linking agent (OTSP) for the stabilization of collagen molecules and the ZnO@Cur nanocomposite for promoting scarless wound healing. DSC and viscosity analysis show improved thermal properties of the hybrid collagen biomaterial due to the interaction of the OTSP and the ZnO@Cur nanocomposite with collagen. FT-IR and CD spectroscopic analyses prove that there are no structural changes in the collagen after interacting with the OTSP and the ZnO@Cur

nanocomposite. The results of hemocompatibility and *in vitro* cell-line studies show that the prepared hybrid collagen scaffolds are suitable for animal studies. The *in vivo* burn wound healing experiments reveal that the hybrid biomaterial enhanced the wound healing with reduced or no scar formation. We propose that the ZnO@Cur nanocomposite in the hybrid scaffold up-regulates angiogenesis and TGF-β3 expression thereby reducing the scar formation. The thickness of the newly regenerated epidermis and the relative SEI value of the hybrid scaffold treated animals demonstrate that the wound is healed without scarring. The *in vitro* and *in vivo* results of this study confirm that the prepared hybrid collagen scaffold is a promising material for scarless wound healing and adequate for further clinical investigations.

Data availability

The raw/processed data required to reproduce these findings cannot be shared at this time due to technical or time limitations.

Conflicts of interest

K. C. and P. T. are inventors on a provisional patent application related to this work filed by the Council of Scientific and Industrial Research (CSIR), New Delhi (Indian Patent Application No. 201811029905; filed on 9 August 2018). The authors declare no other competing interests.

Acknowledgements

K. C. thanks CSIR, New Delhi, for the financial support through the Senior Research Fellowship. The CSIR-CLRI communication number is 1301.

References

1 Z. Fan, B. Liu, J. Wang, S. Zhang, Q. Lin, P. Gong, L. Ma and S. Yang, *Adv. Funct. Mater.*, 2014, **24**, 3933–3943.
2 S. Y. Asadi, P. Parsaei, M. Karimi, S. Ezzati, A. Zamiri, F. Mohammadizadeh and M. Rafieian-kopaei, *Int. J. Surg.*, 2013, **11**, 332–337.
3 Y. I. Shen, H. H. G. Song, A. E. Papa, J. A. Burke, S. W. Volk and S. Gerecht, *J. Invest. Dermatol.*, 2015, **135**, 2519–2529.
4 F. J. Stoddard Jr., C. M. Ryan and J. C. Schneider, *Surg. Clin. North Am.*, 2014, **94**, 863–878.
5 G. J. Leiros, A. G. Kusinsky, H. Drago, S. Bossi, F. Sturla, M. L. Castellanos, I. Y. Stella and M. E. Balana, *Stem Cells Transl. Med.*, 2014, **3**, 1209–1219.
6 S. Michael, H. Sorg, C. T. Peck, L. Koch, A. Deiwick, B. Chichkov, P. M. Vogt and K. Reimers, *PLoS One*, 2013, **8**, e57741.
7 C. Philandrianos, L. Andrac-Meyer, S. Mordon, J. M. Feuerstein, F. Sabatier, J. Veran, G. Magalon and D. Casanova, *Burns*, 2012, **38**, 820–829.
8 S. Ullah, I. Zainol, S. R. Chowdhury and M. B. Fauzi, *Int. J. Biol. Macromol.*, 2018, **111**, 158–168.
9 W. K. Griera, A. S. Tiffanya, M. D. Ramsey and B. A. C. Harley, *Acta Biomater.*, 2018, **76**, 116–125.
10 M. Quade, M. Schumacher, A. Bernhardt, A. Lode, M. Kampschulte, A. Vob, P. Simond, O. Uckermann, M. Kirsch and M. Gelinsky, *Mater. Sci. Eng., C*, 2018, **84**, 159–167.
11 A. Tidu, D. Ghoubay-Benallaoua, C. Teulon, S. Asnacios, K. Grieve, F. Portier, M. C. Schanne-Klein, V. Borderie and G. Mosser, *Biomater. Sci.*, 2018, **6**, 1492–1502.
12 L. L. H. Huang-Lee, D. T. Cheung and M. E. Nimni, *J. Biomed. Mater. Res.*, 1990, **24**, 1185–1201.
13 Y. Yang, A. C. Ritchie and N. M. Everitt, *Mater. Sci. Eng., C*, 2017, **80**, 263–273.
14 R. Murali, P. Thanikaivelan and K. Cheirmadurai, *Carbohydr. Polym.*, 2014, **114**, 399–406.
15 R. Murali, P. Thanikaivelan and K. Cheirmadurai, *J. Mater. Chem. B*, 2016, **4**, 5850–5862.
16 C. Chandra Mohan, K. Harini, B. V. Aafrin, U. Lalitha Priya, P. Maria Jenita, S. Babuskin, S. Karthikeyan and M. Sukumar, *Carbohydr. Polym.*, 2018, **186**, 394–401.
17 A. Ajovalasit, M. A. Sabatino, S. Todaro, S. Alessi, D. Giacomazza, P. Picone, M. Di Carlo and C. Dispenza, *Carbohydr. Polym.*, 2018, **179**, 262–272.
18 V. Kant, D. Kumar, R. Prasad, A. Gopal, N. N. Pathak, P. Kumar and S. K. Tandan, *J. Surg. Res.*, 2017, **212**, 130–145.
19 J. Liu, Z. Chen, J. Wang, R. Li, T. Li, M. Chang, F. Yan and Y. Wang, *ACS Appl. Mater. Interfaces*, 2018, **10**, 16315–16326.
20 K. L. Kaufman, F. A. Mann, D. Y. Kim, S. Lee and H. Y. Yoon, *Vet. Surg.*, 2014, **43**, 972–982.
21 M. Binnebosel, J. Grommes, B. Koenen, K. Junge, C. D. Klink, M. Stumpf, A. P. Öttinger, V. Schumpelick, U. Klinge and C. J. Krones, *Int. J. Colorectal. Dis.*, 2010, **25**, 251–257.
22 S. A. Mansour and A. H. Mossa, *Pestic. Biochem. Physiol.*, 2010, **96**, 14–23.
23 C. K. Simi and T. E. Abraham, *Food Hydrocolloids*, 2010, **24**, 72–80.
24 G. Gorczyca, R. Tylingo, P. Szweda, E. Augustin, M. Sadowska and S. Milewski, *Carbohydr. Polym.*, 2014, **102**, 901–911.
25 S. Sowmya and N. N. Fathima, *ACS Appl. Mater. Interfaces*, 2017, **9**, 5916–5926.
26 H. Liu, X. Li, X. Niu, G. Zhou, P. Li and Y. Fan, *Biomacromolecules*, 2011, **12**, 2914–2924.
27 H. Chhabra, R. Deshpande, M. Kanitkar, A. Jaiswal, V. P. Kaleb and J. R. Bellare, *RSC Adv.*, 2016, **6**, 1428–1439.
28 S. Liu, L. Jiang, H. Li, H. Shi, H. Luo, Y. Zhang, C. Yu and Y. Jin, *J. Invest. Dermatol.*, 2014, **134**, 2648–2657.
29 T. J. Bootten, P. J. Harris, L. D. Melton and R. H. Newman, *J. Exp. Bot.*, 2004, **55**, 571–583.
30 N. Lucyszyn, A. F. Lubambo, K. F. Matos, I. Marvilla, C. F. Souza and M. R. Sierakowski, *Mater. Sci. Eng., C*, 2009, **29**, 552–558.
31 E. Zhang, J. Li, Y. Zhou, P. Che, B. Ren, Z. Qin, L. Ma, J. Cui, H. Sun and F. Yao, *Acta Biomater.*, 2017, **55**, 420–433.
32 J. F. Mukerabigwi, S. Lei, H. Wang, S. Luo, X. Ma, J. Qin, X. Huang and Y. Cao, *RSC Adv.*, 2015, **5**, 83732–83742.

33 P. Fageria, S. Gangopadhyay and S. Pande, *RSC Adv.*, 2014, **4**, 24962–24972.
34 D. Bagchi, T. K. Maji, S. Sardar, P. Lemmens, C. Bhattacharya, D. Karmakare and S. K. Pal, *Phys. Chem. Chem. Phys.*, 2017, **19**, 2503–2513.
35 R. N. Moussawi and D. Patra, *RSC Adv.*, 2016, **6**, 17256–17268.
36 K. Cheirmadurai, P. Thanikaivelan and R. Murali, *Carbohydr. Polym.*, 2016, **137**, 584–593.
37 M. Zhang, C. Ding, J. Yang, S. Lin, L. Chen and L. Huang, *Carbohydr. Polym.*, 2016, **137**, 410–417.
38 I. Kanungo, N. N. Fathima, J. R. Rao and B. U. Nair, *Phys. Chem. Chem. Phys.*, 2015, **17**, 2778–2793.
39 E. Badea, G. D. Gatta and T. Usacheva, *Polym. Degrad. Stab.*, 2012, **97**, 346–353.
40 T. Qiang, L. Chen, Q. Zhang and X. Liu, *J. Cleaner Prod.*, 2018, **197**, 1117–1123.
41 Q. Liang, L. Wang, Y. He, Z. Wang, J. Xu and H. Ma, *J. Funct. Foods*, 2014, **11**, 493–499.
42 N. Alexandre, J. Ribeiro, A. Gartner, T. Pereira, I. Amorim, J. Fragoso, A. Lopes, J. Fernandes, E. Costa, A. Santos-Silva, M. Rodrigues, J. D. Santos, A. C. Maurıcio and A. L. Luis, *J. Biomed. Mater. Res., Part A*, 2014, **102**, 4262–4275.
43 J. Hoppstädter, N. Hachenthal, J. V. Valbuena-Perez, S. Lampe, K. Astanina, M. M. Kunze, S. Bruscoli, C. Riccardi, T. Schmid, B. Diesel and A. K. Kiemer, *J. Biol. Chem.*, 2016, **291**, 22949–22960.
44 R. Guo, A. R. Merkel, J. A. Sterling, J. M. Davidson and S. A. Guelcher, *Biomaterials*, 2015, **73**, 85–95.
45 C. Mohanty, M. Das and S. K. Sahoo, *Biomaterials*, 2010, **31**, 6597–6611.
46 S. C. Gupta, S. Prasad, J. H. Kim, S. Patchva, L. J. Webb, I. K. Priyadarsini and B. B. Aggarwal, *Nat. Prod. Rep.*, 2011, **28**, 1937–1955.
47 T. Mitra, P. J. Manna, S. T. K. Raja, A. Gnanamani and P. P. Kundu, *RSC Adv.*, 2015, **5**, 98653–98665.
48 P. T. Sudheesh Kumar, V. K. Lakshmanan, T. V. Anilkumar, C. Ramya, P. Reshmi, A. G. Unnikrishnan, S. V. Nair and R. Jayakumar, *ACS Appl. Mater. Interfaces*, 2012, **4**, 2618–2629.
49 V. Kant, A. Gopal, D. Kumar, N. N. Pathak, M. Ram, B. L. Jangir, S. K. Tandan and D. Kumar, *J. Surg. Res.*, 2015, **193**, 978–988.
50 W. Chen, X. Fu, S. Ge, T. Sun, G. Zhou, D. Jiang and Z. Sheng, *Wound Repair Regen.*, 2005, **13**, 68–75.
51 T. T. Phan, L. Sun, B. H. Bay, S. Y. Chan and S. T. Lee, *J. Trauma*, 2003, **54**, 1212–1224.
52 S. Moshref, *Egypt. J. Surg.*, 2006, **25**, 169–177.
53 B. Bandyopadhyay, J. Fan, S. Guan, Y. Li, M. Chen, D. T. Woodley and W. Li, *J. Cell Biol.*, 2006, **172**, 1093–1105.
54 T. Tsukazaki, T. A. Chiang, A. F. Davison, L. Attisano and J. L. Wrana, *Cell*, 1998, **95**, 779–791.
55 L. Jiao, C. C. Wang, H. Wu, R. Gong, F. H. Lin, J. Feng and C. Hu, *Innate Immun.*, 2017, **23**, 648–655.